A Flow-Diffusion Model of Oxygen Transport for Quantitative Mapping of Cerebral Metabolic Rate of Oxygen ($CMRO_2$) with Single Gas Calibrated fMRI

Chiarelli A.M.[1,2*], Germuska M.[3*], Chandler H.L.[3], Stickland R.C.[4], Patitucci E.[3]. Biondetti E.[1,2], Mascali D.[1,2], Saxena N. [3], Khot S. [3], Steventon J.[3], Foster C. [5], Rodríguez-Soto A.E.[6], Englund E.[7], Murphy K[3], Tomassini V. [1,2,3,,8], Wehrli F.W.[9], Wise R.G. [1,2,3]

[1] *Department of Neuroscience, Imaging, and Clinical Sciences, University G. D'Annunzio of Chieti-Pescara, Via Luigi Polacchi 13, Chieti, Italy, 66100*

[2] *Institute for Advanced Biomedical Technologies, University G. D'Annunzio of Chieti-Pescara, Via Luigi Polacchi 13, Chieti, Italy, 66100*

[3] *Cardiff University Brain Research Imaging Centre (CUBRIC), Department of Psychology, Cardiff University, Cardiff, United Kingdom*

[4] *Physical Therapy and Human Movement Sciences, Feinberg School of Medicine, Northwestern University, Chicago, IL, United States*

[5] *Wales Institute of Social and Economic Research and Data (WISERD), School of Social Sciences, Cardiff University, Cardiff, UK.*

[6] *Department of Radiology, University of California, San Diego, La Jolla, California, USA*

[7] *Department of Radiology, University of Colorado, Aurora, Colorado, USA.*

[8] *MS Centre, Dept of Clinical Neurology, SS. Annunziata University Hospital, Chieti, Italy*

[8] *Institute of Psychological Medicine and Clinical Neurosciences, Cardiff University, Cardiff, UK*

[8]*Helen Durham Centre for Neuroinflammation, University Hospital of Wales, Cardiff, UK*

[9] *Department of Radiology, University of Pennsylvania, Philadelphia, Pennsylvania, USA.*

** These authors contributed equally to this work*

Corresponding Author:

Dr. Antonio Maria Chiarelli. Ph.D.

University ‘G. d’Annunzio’ of Chieti-Pescara

Institute for Advanced Biomedical Technologies

Via Luigi Polacchi 11, Chieti, Italy, 66100

Email: antonio.chiarelli@unich.it

Orcid ID: https://orcid.org/0000-0002-5347-8417

Running Headline: Mapping $CMRO_2$ with O_2 Transport Model and fMRI

Authors’ Emails: antonio.chiarelli@unich.it,

GermuskaM@cardiff.ac.uk,

ChandlerHL1@cardiff.ac.uk

rachael.stickland@northwestern.edu,

PatitucciE@cardiff.ac.uk

emma.biondetti@unich.it,

daniele.mascali@unich.it,

saxenan2@cardiff.ac.uk

KhotS@cardiff.ac.uk

steventonjj@cardiff.ac.uk

fosterc6@cardiff.ac.uk

arivleana@gmail.com,

erin.englund@cuanschutz.edu,

murphyk2@cardiff.ac.uk

valentina.tomassini@unich.it

Felix.Wehrli@pennmedicine.upenn.edu,

richard.wise@unich.it

Abstract

One promising approach for mapping $CMRO_2$ is dual-calibrated functional MRI (dc-fMRI). This method exploits the Fick Principle to combine estimates of resting CBF from ASL, and resting OEF derived from BOLD-ASL measurements during arterial O_2 and CO_2 modulations. Multiple gas modulations are required to decouple OEF and deoxyhemoglobin-sensitive blood volume. We propose an alternative single gas calibrated fMRI framework, integrating a model of oxygen transport, that links blood volume and CBF to OEF and creates a mapping between the maximum BOLD signal, CBF, and OEF (and $CMRO_2$). Simulations demonstrated the method's viability within mitochondrial oxygen pressure, P_mO_2, and mean capillary transit time physiological ranges. A dc-fMRI experiment, performed on 20 healthy subjects using alternating O_2 and CO_2 challenges, was used to validate the approach. The validation conveyed expected estimates of model parameters (e.g., low P_mO_2), with stable OEF maps (grey matter, GM, OEF Standard Deviation≈0.13). GM OEF estimates obtained with hypercapnia correlated with dc-fMRI ($r=0.65$, $p=2\cdot10^{-3}$). For 12 subjects, OEF measured with dc-fMRI and the single gas calibration method were correlated with whole-brain OEF derived from phase measures in the superior sagittal sinus ($r=0.58$, $p=0.048$; $r=0.64$, $p=0.025$ respectively). The simplified calibrated fMRI method using hypercapnia holds promise for clinical application.

Keywords: Calibrated Functional Magnetic Resonance Imaging (Calibrated fMRI), Cerebral Metabolic Rate of Oxygen ($CMRO_2$), Hypercapnia, Hyperoxia, Oxygen Transport Modelling

INSERT TABLE 1 HERE

1. Introduction

Oxidative metabolism provides most of the brain's energy and is altered in a variety of pathologies such as neurodegenerative and neuroinflammatory diseases, stroke, epilepsy, and migraine[1]. Magnetic resonance imaging (MRI) approaches for mapping baseline ($_0$) cerebral metabolic rate of oxygen ($CMRO_{2,0}$)[2–8] exploit the Fick Principle, that expresses $CMRO_2$ as the product of oxygen delivery (the product of oxygen concentration in arterial blood, C_aO_2, and cerebral blood flow, CBF) and oxygen extraction fraction (OEF) measured in either the macrovascular or the microvascular compartment. Macrovascular CBF_0 can be estimated from volume flow rate in large feeding arteries or draining veins using flow encoding sequences[2], whereas OEF_0 can be assessed in draining veins using sequences that measure magnetic susceptibility or blood T_2 predominantly affected by the presence of deoxyhemoglobin (dHb)[8,9]. Since large vessels feed or drain significant portions of brain, such measures deliver global or regional information at best. Microvascular CBF_0 can be mapped using perfusion-weighted sequences such as Arterial Spin Labelling (ASL). One drawback of ASL is its low contrast in white matter (WM). Moreover, mapping microvascular OEF_0 is challenging because baseline magnetic susceptibility and MR relaxation parameters within a voxel with a small vascular compartment are not uniquely affected by dHb.

Among others[10,11], dual-calibrated functional MRI (dc-fMRI)[4,12–15] is a promising approach for OEF_0 and $CMRO_{2,0}$ mapping. While measuring CBF_0 with ASL, dc-fMRI estimates OEF_0 from the blood oxygen level dependent (BOLD) signal sensitivity to dHb_0. dc-fMRI uses BOLD-ASL recordings, biophysical modelling of BOLD signal[16] and assumed isometabolic hypercapnic and hyperoxic modulations of CBF and C_aO_2 through respiratory stimuli. BOLD sensitivity to dHb_0 is encoded in the maximum BOLD increase, M, corresponding to complete dHb removal. The two respiratory stimuli decouple the contribution to M of OEF_0 and the dHb_0-sensitive cerebral blood volume, $CBV_{v,0}$, when Hb concentration in blood [Hb][4,14] is known. Although dc-fMRI has been applied in exemplar clinical studies[17–21], its adoption is limited by the low signal to noise ratio (SNR)[22] and by the complex gas challenge paradigm required.

Here, we introduce a new calibrated fMRI framework that estimates OEF_0 with only one measurement of M based on one manipulation of brain physiology and a flow-diffusion model of oxygen transport[13,23,24]. The model

describes the steady-state oxygen diffusion from the capillaries into the tissue (equal to $CMRO_2$) as proportional to the product of the mean capillary transit time (mean CTT, MCTT) and the pressure gradient between the capillary bed and the mitochondria (where the proportionality constant is the effective tissue permeability to oxygen, k). Since MCTT can be expressed as the ratio between capillary blood volume (CBV_{cap}) and CBF, the flow-diffusion model can be incorporated in the formulation of M by substituting $CBV_{v,0}$ for an appropriately scaled $CBV_{cap,0}$ (with ρ being the scaling factor). This substitution replaces one unknown variable, $CBV_{v,0}$, with two unknowns, one proportionality constant, being a function of ρ and k, and the oxygen pressure at the mitochondria ($P_mO_{2,0}$). The advantage of the model lies in the tight distributions of the new parameters and on the reduced effect of their variabilities in the estimate of OEF_0, creating a probabilistic mapping of M, $C_aO_{2,0}$ and CBF_0 with OEF_0 and $CMRO_{2,0}$ as the parameters to be inferred.

This manuscript reports the validation of the novel single gas approach. We term the new approach using a hypercapnic stimulus, hc-fMRI+, and that using a hyperoxic stimulus, ho-fMRI+. The report is divided into four sections. The first section, by exploiting simulations, describes the advantages, the validity, and the robustness to noise of the framework. The second section investigates the new model *in-vivo* using a dc-fMRI experiment, employing alternating hypercapnic and hyperoxic gas challenges in healthy subjects. We use a global estimate of OEF_0 in the grey matter (GM), obtained with dc-fMRI analysis[22], and we invert the single gas model using only the hypercapnic or the hyperoxic component of the experiment to investigate the distribution of the proportionality constant and $P_mO_{2,0}$ across subjects. The third section validates hc-fMRI+ and ho-fMRI+ against dc-fMRI[22]. To do so, the two parameters of the model are fixed to the average values obtained from the previous analysis, and the model is inverted to infer OEF_0. Finally, in the fourth section, GM OEF_0 estimates from the different fMRI approaches are compared to whole-brain OEF_0 inferred from a validated MRI sequence performing phase measures in the superior sagittal sinus (SSS) and conventionally termed 'OxFlow'[2,25].

2. Methods

2.1. Analytical Modeling

Here we summarize the analytical model derivation. Please refer to Supplementary Information for a more detailed description.

2.1.1. BOLD Model and the Dual-Calibrated fMRI Experiment

The rate of signal decay due to dHb, $R_2^*|_{dHb}$, within a voxel is represented by[26,27]:

$$R_2^*|_{dHb} = \mathrm{A} \cdot CBV_v \cdot \left((1 - S_vO_2) \cdot [Hb]\right)^{\beta} \quad (1)$$

where S_vO_2 is venous saturation, [Hb] is the concentration of hemoglobin in blood and CBV_v is the BOLD sensitive blood volume. β (β =1.3 at 3T) and A are field strength and vessel geometry dependent constants. For small perturbations of $R_2^*|_{dHb}$ and using the Grubb relation linking fractional changes in CBV_v and CBF, the steady-state BOLD signal can be expressed, within the Davis Model framework, as[14,28]:

$$\frac{\Delta BOLD}{BOLD_0} = TE \cdot A \cdot CBV_{v,0} \cdot \left(\left(1 - S_vO_{2,0}\right) \cdot [Hb]\right)^{\beta} \cdot \left\{1 - \left(\frac{CBF}{CBF_0}\right)^{\alpha} \cdot \left(\frac{1-S_vO_2}{1-S_vO_{2,0}}\right)^{\beta}\right\} \quad (2)$$

with the maximum BOLD signal M being equal to:

$$M = TE \cdot A \cdot CBV_{v,0} \cdot \left(\left(1 - S_vO_{2,0}\right) \cdot [Hb]\right)^{\beta} \quad (3)$$

The subscript $_0$ depicts baseline values, $\Delta BOLD/BOLD_0$ is the relative BOLD signal change, TE is the sequence echo-time and α is the Grubb exponent (α =0.38). During an isometabolic manipulation of brain physiology, Equation 2 can be expressed as a function of OEF_0 as:

$$\frac{\Delta BOLD}{BOLD_0} = TE \cdot A \cdot CBV_{v,0} \cdot \left(\left(1 - \frac{C_aO_{2,0}}{\varphi \cdot [Hb]} \cdot (1 - OEF_0)\right) \cdot [Hb]\right)^{\beta} \cdot \left\{1 - \left(\frac{CBF}{CBF_0}\right)^{\alpha} \cdot \left(\frac{1 - \frac{C_aO_2}{\varphi \cdot [Hb]} \cdot \left(1 - \frac{OEF_0 \cdot CBF_0 \cdot C_aO_{2,0}}{CBF \cdot C_aO_2}\right)}{1 - \frac{C_aO_2}{\varphi \cdot [Hb]} \cdot (1 - OEF_0)}\right)^{\beta}\right\} \quad (4)$$

with C_aO_2 being the oxygen concentration in arterial blood and φ being the oxygen binding capacity of hemoglobin (φ =1.34 mL/g). Even when combining together A and $CBV_{v,0}$ in Equation 4, the equation still has two unknowns making it not possible to solve for OEF_0 through one manipulation of brain physiology. dc-fMRI solves this by performing two independent manipulations: hypercapnia and hyperoxia. However, the approach suffers from low SNR, a problem that has been addressed by regularizing the inversion procedure for OEF_0[29] and by using, simulation-trained, machine learning approaches applied to raw recordings[22].

2.1.2. Flow-Diffusion Model of Oxygen Transport

A simple model can be used to describe the steady-state radial oxygen diffusion into the tissue along a straight cylindrical capillary of unit length[24]:

$$\frac{dC_{cap}O_2(x)}{dx} = -k \cdot T_{cap} \cdot (P_{cap}O_2(x) - P_mO_2) \quad (5)$$

where $C_{cap}O_2$ and $P_{cap}O_2$ are the concentration and the partial pressure of oxygen at a relative position x along the capillary and T_{cap} is the CTT. k, the effective permeability, combines the effects of the capillary wall and the surrounding brain tissue into a single interface between the plasma and a well-stirred oxygen pool at the mitochondria at end of the diffusion path, at which the pressure of oxygen is equal to P_mO_2[13,30]. CTT in the single straight capillary is then approximated by the MCTT in the capillary bed within the voxel. MCTT is expressed as the ratio between the capillary blood volume (CBV_{cap}) and CBF. Since $P_{cap}O_2$ and $C_{cap}O_2$ quickly equilibrate (less than a few milliseconds), depending upon the nonlinear nature of Hb binding to oxygen described mathematically by the Hill Equation:

$$SO_2 = \frac{1}{1+\left(\frac{P_{50}}{PO_2}\right)^h} \quad (6)$$

the following can be obtained:

$$CBF \cdot \frac{dC_{cap}O_2(x)}{dx} = -k \cdot CBV_{cap} \cdot \left(P_{50} \cdot \sqrt[h]{\frac{C_{cap}O_2(x)}{\varphi \cdot [Hb] - C_{cap}O_2(x)}} - P_mO_2\right) \quad (7)$$

where P_{50} is the oxygen partial pressure when half of Hb is saturated (generally P_{50}≈26 mmHg; P_{50} can be inferred from a measure of end-tidal partial pressure of carbon dioxide, $P_{ET}CO_2$), and h is the Hill constant (h=2.8). An approximated closed solution to the differential Equation 7 can be made assuming a linear decrease of $C_{cap}O_2(x)$ and an average $C_{cap}O_2(x)$ equal to $\langle C_{cap}O_2(x)\rangle \approx \varphi \cdot [Hb] \cdot (S_aO_2 + S_vO_2)/2 = \varphi \cdot [Hb] \cdot (1 - OEF/2)$, where S_aO_2 is the arterial oxygen saturation. Integrating Equation 7 and equalizing the oxygen loss from the capillary to $CMRO_2$, the following is obtained:

$$CMRO_2 = CBF \cdot OEF \cdot CaO_2 = k \cdot CBV_{cap} \cdot \left(P_{50} \cdot \sqrt[h]{\frac{2}{OEF} - 1} - P_mO_2\right) \quad (8)$$

2.1.3. Integration of the Flow-Diffusion Model of Oxygen Transport into the BOLD Model for Calibrated-fMRI Quantification of $CMRO_2$

CBV_{cap} is here assumed to be a fraction of CBV_v, i.e., $CBV_v=\rho\cdot CBV_{cap}$. Substituting CBV_{cap}, from Equation 8 into Equation 4, we obtain:

$$\frac{\Delta BOLD}{BOLD_0} = TE\cdot\frac{A\cdot\rho}{K}\cdot\frac{CBF_0\cdot OEF_0\cdot CaO_{2,0}\cdot\left(\left(1-\frac{C_aO_{2,0}}{\varphi[Hb]}\cdot(1-OEF_0)\right)\cdot[Hb]\right)^{\beta}}{\left(P_{50}\cdot{}^{h}\sqrt{\frac{2}{OEF_0}-1}-P_mO_{2,0}\right)}\cdot\left\{1-\left(\frac{CBF}{CBF_0}\right)^{\alpha}\cdot\left(\frac{1-\frac{C_aO_2}{\varphi[Hb]}\cdot\left(1-\frac{OEF_0\cdot CBF_0\cdot C_aO_{2,0}}{CBF\cdot C_aO_2}\right)}{1-\frac{C_aO_{2,0}}{\varphi[Hb]}\cdot(1-OEF_0)}\right)^{\beta}\right\} \quad (9)$$

with the maximum BOLD signal M equal to:

$$M = TE\cdot\frac{A\cdot\rho}{K}\cdot\frac{CBF_0\cdot OEF_0\cdot CaO_{2,0}\cdot\left(\left(1-\frac{C_aO_{2,0}}{\varphi[Hb]}\cdot(1-OEF_0)\right)\cdot[Hb]\right)^{\beta}}{\left(P_{50}\cdot{}^{h}\sqrt{\frac{2}{OEF_0}-1}-P_mO_{2,0}\right)} \quad (10)$$

Equations 9 and 10 encode a non-linear mapping of measurable quantities M, $C_aO_{2,0}$ and CBF_0 with OEF_0, enabling OEF_0 (and hence $CMRO_{2,0}$) to be inferred using a single manipulation of brain physiology. Apart from the constants that can be indirectly inferred (e.g., P_{50}, [Hb]), assumed (e.g., φ, β) or controlled (e.g., TE), the mapping depends on the non-measurable quantities: A, ρ, k and $P_mO_{2,0}$. A, having the same origins as β[31], can be estimated assuming primarily an extravascular BOLD signal and assuming $R_2^*|_{dHb} = R_2'$[32,33]. With an experimentally determined cortical R_2' of approximately 3 s^{-1} at 3T[34], an average [Hb] of 14 g/dL, a S_vO_2 of 0.6, and a mean CBV_v of 2.5%, from Equation 1 we expect a value of A≈14 $s^{-1}g^{-\beta}dL^{\beta}$ at 3T. *In-vivo* variation in ρ has not been studied directly; we discuss this in the Supplementary Information. We expect ρ to be in the range 2 to 3, assuming a capillary blood volume between 20% to 40% of total blood volume, when the arterial contribution is assumed to be 20% to 30%[35]. Moreover, we expect a value for the oxygen effective permeability k of around 3 μmol/mmHg/ml/min[22]. This value is derived from the literature using a different formalism where oxygen diffusion is assumed to happen at the endothelial wall of capillaries[36]. In Equations 9 and 10, we create a practical grouping of A, ρ and k into one multiplicative parameter A·ρ/k. At a fixed field strength, all the three parameters are related to tissue structure and vessel geometry, which plausibly affects water and oxygen diffusion in the intravascular and extravascular spaces as well as the volumetric relationship between capillaries, venules and veins. We expect a

value of $A\cdot\rho/k$ of the order of $A\cdot\rho/k\approx10\ s^{-1}g^{-\beta}dL^{\beta}/(\mu mol/mmHg/ml/min)$. The mitochondrial oxygen partial pressure at rest, $P_mO_{2,0}$, must lie between 0 mmHg and the average oxygen tension of the capillary bed. Several in vivo studies suggest that oxygen tension at brain mitochondria is small in the healthy brain[23,37], and this theory is consistent with functional hyperemia in response to increased brain oxygen demand. However, departure from a negligible oxygen tension is plausible in the diseased brain.

In summary, the non-linear mapping in Equation 9 permits estimation of OEF_0 from one manipulation of brain physiology. Uncertainty in the mapping is driven by variability in two non-measurable quantities, a proportionality constant $A\cdot\rho/k$, that depends on tissue and micro-vessel structure at a fixed field strength, and $P_mO_{2,0}$. Importantly, these non-measurable quantities affect the non-linear mapping differently. The advantage of the new framework lies in the low variability of these parameters and their diminished influence on the OEF_0 estimation compared to $CBV_{v,0}$.

2.2. Simulations (Section 1)

We performed simulations to investigate the ability of hc-fMRI+ and ho-fMRI+ to infer OEF_0. A forward model using Equation 9 was implemented to simulate the BOLD signal and was inverted to retrieve OEF_0. In the forward model some variables were fixed (TE, α, β, h ε, φ) (ε is the oxygen plasma solubility, ε=0.0031 mL/mmHg/dL) while others were simulated based on random sampling from physiologically and physically plausible distributions. When inverting the model, some random variables were unknown and were either fixed a-priori ($A\cdot\rho/k$, $P_mO_{2,0}$), or inferred (OEF_0, $CBV_{cap,0}$ and $MCTT_{,0}$). Firstly, we ran the full forward and inverse analysis without measurement noise as a function of either the value chosen a-priori for the random variables that were fixed during the inversion or other parameters of interest ($P_mO_{2,0}$ and $MCTT_{,0}$). Secondly, we evaluated the effect of measurement noise, which was introduced on measures with lower signal to noise ratio (SNR), namely ASL CBF/CBF_0 and $\Delta BOLD/BOLD_0$. 10^7 simulations per condition were conducted; the non-linear inversions were performed through explicit search of OEF_0 that explained the measures. The explicit search was performed in the full OEF_0 space (between 0 and 1) with a resolution of 0.01. Constant parameters were set to α=0.38, β=1.3, h=2.8, ε=0.0031 mL/mmHg/dL, φ=1.34 mL/g, TE= 30 ms, whereas random variables were simulated using either normal (N) or

gamma (Γ) distributions; additional physiological constraints were applied (please refer to the Table in Supplementary Information for additional information).

Figure 1 reports the distributions of the main random variables used in the forward model simulations. With respect to the parameters that were not measured for the inversion, $A \cdot \rho/k$ was simulated using a normal distribution with an average value of 10 $s^{-1}g^{-\beta}dL^{\beta}/(\mu mol/mmHg/ml/min)$ and a coefficient of variation (CoV) of 0.3, whereas $P_mO_{2,0}$ was simulated using a gamma distribution, allowing variation between zero and $<P_{cap,0}>$ to simulate a large variability in $P_mO_{2,0}$ that might be present in disease.

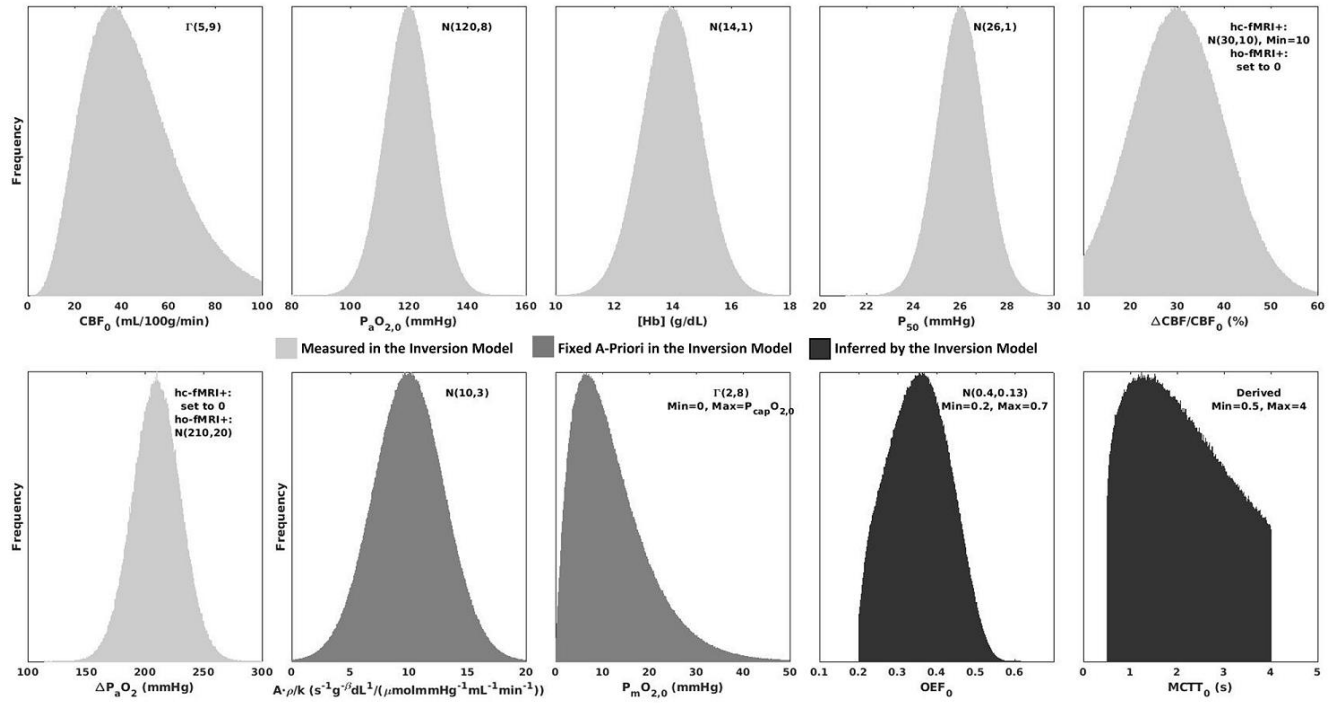

Figure 1: Random variables used to simulate BOLD and ASL signals using a hc-fMRI+ or ho-fMRI+ forward modelling framework. The variables reported in light grey were assumed to be measured for the hc-fMRI+ or ho-fMRI+ inversion model, those reported in medium grey were fixed a-priori in the inversion model and those in dark grey were inferred by the inversion model.

2.3. MRI Experiment (Sections 2-3-4)

Twenty healthy volunteers (13 males, mean age 31.9 ± 6.5 years) were recruited at CUBRIC, Cardiff University, Cardiff, UK. The study was in accordance with the Declaration of Helsinki and was approved by the Cardiff University, School of Psychology Ethics Committee and NHS Research Ethics Committee, Wales, UK.

Written consent was obtained from each participant. Data were acquired using a Siemens MAGNETOM Prisma (Siemens Healthcare GmbH, Erlangen) 3T clinical scanner with a 32-channel receiver head coil (Siemens Healthcare GmbH, Erlangen). A 18 minutes dc-fMRI scan was acquired with interleaved periods of hypercapnia, hyperoxia and medical air being delivered according to the protocol previously proposed[13,29]. 3 periods of hypercapnic gas challenges and 2 periods of hyperoxic gas challenges were performed. CO_2 and O_2 in the lungs were evaluated from the volunteer's facemask using a gas analyzer (AEI Technologies, Pittsburgh, PA, USA).

Calibrated fMRI data were acquired during the gas challenge scheme using a pCASL acquisition with pre-saturation and background suppression[38] and a dual-excitation (DEXI) readout[39]. The labelling duration (τ) and the Post Label Delay (PLD) were both set to 1.5 s, GRAPPA acceleration (factor = 3) was used with TE_1 = 10 ms and TE_2 = 30 ms. An effective TR of 4.4 s was used to acquire 15 slices, in-plane resolution 3.4 mm×3.4 mm and slice thickness 7 mm with a 20% slice gap. A calibration (S_0) image was acquired for ASL quantification with pCASL labelling and background suppression pulses switched off, with TR=6 s, and TE =10 ms[13]. A high-resolution whole brain structural image, used for GM identification in the fMRI space, was acquired using a 3D Fast Spoiled Gradient-Recalled-Echo T1-weighted acquisition (resolution = 1×1×1 mm^3, TE = 3.0 ms, TR = 7.8 ms, TI = 450 ms, flip angle=20˚).

For susceptometry-based oximetry, a transverse slice was acquired at approximately 15 mm above the confluence of sinuses (location at which the inferior sagittal, straight, and transverse sinuses join the SSS) using a T2*-weighted spoiled multi-echo gradient-recalled echo (GRE) sequence with: in-plane resolution = 1.6×1.6 mm^2, slice thickness = 5 mm, field of view (FOV) = 208×208 mm^2, bandwidth= 260 Hz/pixel, three echo times (TEs = 3.92, 7.44, and 10.96 ms), bipolar gradient readout, TR = 35 ms, flip angle = 25˚, and acquisition time = 1 min and 7 s. This acquisition was performed in the framework of the OxFlow method, which previous studies have described in detail[40–42]. For vessel identification purposes, two-dimensional T2*-weighted time-of-flight (TOF) images were acquired using a spoiled GRE sequence with: in-plane resolution = 0.86×0.86 mm^2, slice thickness = 2 mm, slice gap = 1.34 mm, FOV = 219×219×234 mm^3, in-plane acceleration factor = 2, bandwidth = 220 Hz/pixel, TE=4.99

ms, TR =20 ms, flip angle=60˚. Blood samples were drawn via a finger prick before scanning and were analyzed with the HemoCue Hb 301 System (HemoCue, Ängelholm, Sweden) to calculate [Hb].

2.4. fMRI Data Processing (Section 2-3)

2.4.1. Gas Recordings Processing

$P_{ET}CO_2$ and $P_{ET}O_2$ were extracted from CO_2 and O_2 recordings using in-house software in Matlab (Mathworks, Natick, MA). $P_{ET}CO_2$ and $P_{ET}O_2$ points were interpolated (cubic spline function), resampled to match fMRI, and shifted in time to maximally correlate with fMRI signals. $P_{ET}CO_{2,0}$ and $P_{ET}O_{2,0}$, were evaluated at baseline in the first 110 seconds. $P_{ET}O_2$ was assumed equal to PaO_2 for C_aO_2 computation whereas $P_{ET}CO_2$ was assumed equal to $PaCO_2$. P_{50} was inferred from estimates of resting blood pH based on the Henderson-Hasselbalch Equation, assuming $[HCO_3^-]$= 24 mmol/L[43]:

$$pH = 6.1 + \log\left(\frac{[HCO_3^-]}{0.03 \cdot P_aCO_2}\right) \quad (11)$$

and calculating P_{50} according to the linear relation, $P_{50} = 221.87 – 26.37 \cdot pH$[13].

SaO_2 was calculated from PaO_2 using Equation 6 and CaO_2 was inferred using the relation:

$$CaO_2 = \varphi \cdot [Hb] \cdot SO_2 + \varepsilon \cdot PO_2 \quad (12)$$

Finally, to highlight hypercapnic and hyperoxic modulations, $P_{ET}CO_2$ and $P_{ET}O_2$ traces were high-pass filtered with a 4th order Butterworth digital filter and a high-pass frequency of 1/600 Hz.

2.4.2. fMRI Processing

Both functional and structural MRIs were processed using FSL[44] and in-house algorithms implemented in Matlab. fMRI timecourses were motion corrected based on 6 degrees of freedom co-registration using MCFLIRT[45]. High-resolution structural T1-weighted MRIs were skull-stripped using BET[46] and probability maps of Cerebrospinal Fluid (CSF), WM and GM, were computed using FAST[47]. Motion-corrected fMRI timecourses and the skull-stripped T1-weighted MRI, together with tissue probability maps, were coregistered, relying on 12 degrees of freedom affine transformation, to the S_0 image[45]. ASL control-tag difference perfusion data (ΔS) in S_0 space were obtained through surround subtraction of the fMRI timecourses at

TE_1, normalized with respect to S_0 and converted to CBF in quantitative units of ml/100g/min through the pCASL single compartment kinetic model of labelled spins and voxelwise signal normalization[48]:

$$CBF = \frac{6000 \cdot \lambda \cdot e^{\frac{PLD}{T1_b}}}{\eta \cdot \eta_{inv} \cdot T1_b \cdot \left(1 - e^{-\frac{\tau}{T1_b}}\right)} \cdot \left(\frac{\Delta S}{S_0}\right) \quad (13)$$

where λ is the water partition coefficient (λ= 0.9 mL/g), $T1_b$ is the T1 relaxation constant of blood, η is the tagging inversion efficiency (η =0.85), and η_{inv} is a scaling factor to account for the reduction in tagging efficiency due to background suppression (η inv=0.88)[49]. The $T1_b$ was calculated from SaO_2 and PaO_2 measures using the experimental relation presented in[50]:

$$T1_b = \frac{1}{1.527 \cdot 10^{-4} \cdot P_aO_2 + 0.1713 \cdot (1 - S_aO_2) + 0.5848} \quad (14)$$

CBF_0 was evaluated in the first 110 seconds. Finally, fractional CBF was high pass filtered with a 4th order Butterworth digital filter with a high-pass frequency of 1/600 Hz. BOLD T2*-weighted time-courses were obtained through surround averaging of the fMRI at TE_2 and they were expressed as relative BOLD changes with respect to the temporal average of the BOLD signal in the first 110 seconds ($BOLD_0$). BOLD relative changes were high pass filtered with a 4th order Butterworth digital filter with a high-pass frequency of 1/600 Hz.

Both processed CBF and BOLD volumes were masked with a GM mask at 50% probability threshold.

2.4.3. Dual-Calibrated fMRI Analysis

Firstly, OEF_0 maps were obtained with a dc-fMRI analysis. Because of the method's known low SNR, explicit inversion methodologies were avoided and a state-of-the-art method to analyze the data relying on a machine learning approach was used. The machine learning algorithm was fed with fMRI timecourses and, through a time-frequency transformation of fMRI signals to extract features of interest, directly mapped OEF_0 and $CMRO_{2,0}$ relying on a pre-trained model based on simulated data. Please refer to[22] for detailed information.

2.4.4. Single gas calibrated fMRI Analysis

Single gas calibrated fMRI analysis was performed on either the hypercapnic (using hc-fMRI+) or the hyperoxic (using ho-fMRI+) modulations within the dc-fMRI experiment. The evaluation of BOLD and ASL changes with physiological manipulations was performed using the general linear model (GLM)[51]. $P_{ET}CO_2$ and $P_{ET}O_2$ were

concurrently regressed on BOLD and ASL filtered modulations. The GLM β-weight delivered an estimate of BOLD or CBF modulation per unit of mmHg of $P_{ET}CO_2$ and $P_{ET}O_2$. The total modulation was then obtained by multiplying the β-weight with the maximum $P_{ET}CO_2$ or $P_{ET}O_2$ modulation. The SNR of the modulation was estimated by dividing the GLM β-weight by its confidence interval. In section 2 we focus on evaluating the between subjects distribution of the unknown parameters of the extended model, namely $A \cdot \rho/k$ and $P_mO_{2,0}$. This analysis was performed by extracting average BOLD and ASL modulations in the GM. These average estimates were used, together with a global estimate of GM OEF_0 obtained with the dc-fMRI analysis, to invert the model and estimate the unknown parameters. The inversion relied on Equation 9, which clearly could not be solved for the two unknowns; however, since $A \cdot \rho/k$ and $P_mO_{2,0}$ differently affect the non-linear mapping between BOLD and ASL modulations and OEF_0, we were able to get insight into the average value of both parameters. In particular, we inverted the model assessing the proportionality constant $A \cdot \rho/k$ as a function of the a-priori fixed $P_mO_{2,0}$. We expected the $A \cdot \rho/k$ distribution to have a smaller CoV when $P_mO_{2,0}$ was closer to the correct average value. The non-linear inversion was performed through an explicit search in the range, for $A \cdot \rho/k$, between 0 and 40 $s^{-1}g^{-\beta}dL^{\beta}/(\mu mol/mmHg/ml/min)$ with a resolution of 0.2 $s^{-1}g^{-\beta}dL^{\beta}/(\mu mol/mmHg/ml/min)$ and, for $P_mO_{2,0}$, between 0 and 50 mmHg with a resolution of 1 mmHg. In section 3, the unknown parameters were fixed both spatially and between subjects to the optimal values derived in the first step and hc-fMRI+ and ho-fMRI+ inversion models were used for voxelwise estimation of OEF_0 and $CMRO_{2,0}$ and comparison with the estimates derived from the dc-fMRI analysis.

2.5. OxFlow Data Processing (Section 4)

In section 4 of the work, for a subset of twelve subjects, GM estimates of OEF_0 using single or dual calibrated fMRI approaches were compared to whole-brain estimates of OEF_0 from SSS derived using the OxFlow procedure. OxFlow images were processed using Matlab and code developed in-house. OEF_0 measurements were obtained based on the normalized difference in signal phase between the first and third TEs ($\Delta\boldsymbol{\phi}/\Delta TE$), with acquisitions having equal gradient polarity[41]. The static background field inhomogeneity was removed using a second-order polynomial fitting[42]. The intravascular phase was measured as the average signal phase in a region of interest centered in the cross-section of SSS relative to the average signal phase in the tissue region surrounding the SSS. The angle (θ) between the SSS and B_0 was evaluated by comparing the slice acquired for OxFlow and the SSS

orientation in the slices immediately above and immediately below in the TOF image. Individual measurements of hematocrit (Hct, %) were obtained based on [Hb] assuming a ratio Hct/[Hb]=3 (%dL/g)[52].

OEF_0 was calculated using the infinite cylinder analytical model[41]:

$$OEF_0 = \frac{\frac{2\Delta\phi}{\Delta TE}}{\gamma \cdot \Delta\chi_{do} \cdot Hct \cdot B_0 \cdot \left(\cos^2\theta - \frac{1}{3}\right)} \quad (25)$$

where γ is the proton gyromagnetic ratio (γ=267.52·10^6 rad/s/T), and $\Delta\chi_{do}=4\pi\cdot0.27\cdot10^{-6}$ is the magnetic susceptibility difference between fully oxygenated and fully deoxygenated red blood cells[53].

2.6. Statistical Analysis

Pearson's correlations and t-tests were performed to assess pairwise associations and biases between the different estimates. Null-hypothesis probabilities (p-values) were calculated using the Student's t distribution (using transformation of correlation for association testing). Normality evaluation was performed prior to statistical inference using the Kolmogorov-Smirnov test.

3. Results

3.1. Simulations (Section 1)

Figure 2 reports the outcome in estimating OEF_0 when using hc-fMRI+ and ho-fMRI+ inversion models with fixed a-priori parameters. Figure 2a displays the OEF_0 root mean square error (RMSE) obtained for hc-fMRI+ and ho-fMRI+ with $A\cdot\rho/k=10$ $s^{-1}g^{-\beta}dL^{\beta}/(\mu mol/mmHg/ml/min)$ as a function of $P_mO_{2,0}$. A minimum RMSE of $OEF_0=0.039$ was obtained for hc-fMRI+ and a minimum RMSE of $OEF_0=0.051$ was obtained for ho-fMRI+, both at $P_mO_{2,0}=11$ mmHg. Figure 2b displays the scatterplots of the simulated OEF_0 vs. the estimated OEF_0 for hc-fMRI+ and ho-fMRI+ when marginalizing the other variables. The scatterplots reported were obtained using a close to optimal $P_mO_{2,0}$, $P_mO_{2,0}=10$ mmHg, and $P_mO_{2,0}=0$ mmHg. Figure 2c reports the OEF_0 RMSE for the two methods evaluated as a function of two physiological parameters of interest in the forward model, namely $MCTT_0$ and $P_mO_{2,0}$, when fixing a-priori the non-measurable parameters analogous to Figure 2b. Importantly, when adding noise to

BOLD and fractional changes in CBF, the analysis highlighted the stability of the approach with respect to measurement SNR, with the OEF_0 RMSE reaching the OEF_0 RMSE related to model parameters uncertainty at BOLD and ASL SNRs around 4 (refer to Supplementary information for additional information).

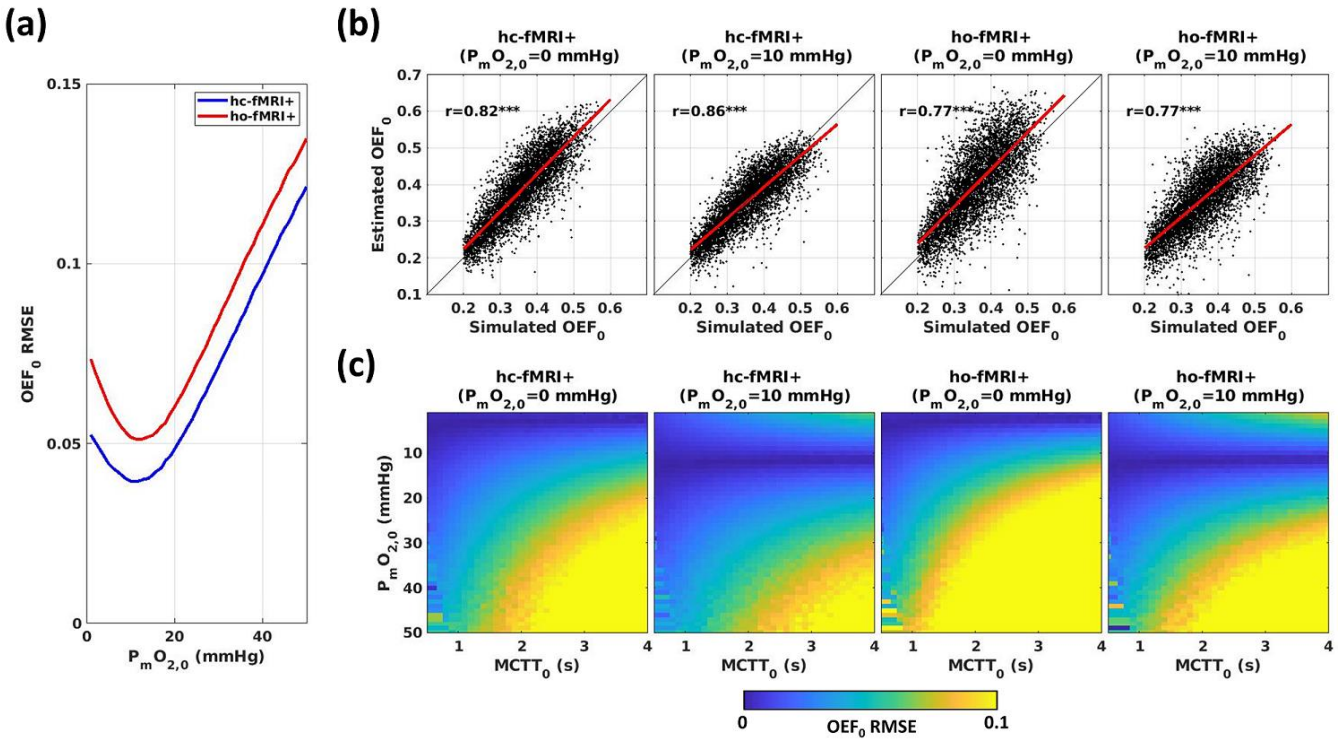

Figure 2: (a) RMSE in OEF_0 for hc-fMRI+ and ho-fMRI+ inversion models with $A \cdot \rho/k=10$ $s^{-1}g^{-\beta}dL^{\beta}/(\mu mol/mmHg/ml/min)$ as a function of $P_mO_{2,0}$. **(b)** Scatterplots of the simulated and estimated OEF_0 for hc-fMRI+ and ho-fMRI+ inversion models assuming either $P_mO_{2,0}$=0 mmHg or $P_mO_{2,0}$=10 mmHg; **(c)** RMSE in OEF_0 as a function of the forward model $MCTT_0$ and $P_mO_{2,0}$ for hc-fMRI+ and ho-fMRI+ inversion models assuming either $P_mO_{2,0}$=0 mmHg or $P_mO_{2,0}$=10 mmHg. *** $p<10^{-3}$

3.2. *In-Vivo* Evaluation of Gas, CBF and BOLD Modulations (Section 2-3-4)

Figure 3 reports the processing steps, in an exemplar subject, that were used to derive the hypercapnic and the hyperoxic CBF and BOLD modulations. Figure 3a shows O_2 signals acquired through the gas analyzer with the estimated $P_{ET}O_2$ traces whereas figure 3b depicts CO_2 signals and $P_{ET}CO_2$ traces. Figure 3c shows example of the ASL CBF/CBF_0 and the filtered and fitted $P_{ET}CO_2$. Figure 3d shows the relative BOLD change and the filtered $P_{ET}CO_2$ and $P_{ET}O_2$ traces fitted onto $\Delta BOLD/BOLD_0$. The GLM β-weight (in units of cerebrovascular reactivity, CVR, or in units of signal per mmHg of $P_{ET}O_2$) were multiplied by the maximum gas modulation to obtain the hypercapnic CBF/CBF_0 and the hypercapnic as well as hyperoxic $\Delta BOLD/BOLD_0$ modulations. Additional

information on gas and signal modulations are reported in the Supplementary Information. The GLM analysis delivered an SNR (evaluated as the statistical relevance of the β-weight) of SNR_{ASL}=6.1 (SD=5.4), hypercapnic SNR_{BOLD}=16 (SD=12.7) and hyperoxic SNR_{BOLD}=8.6 (SD=7.52).

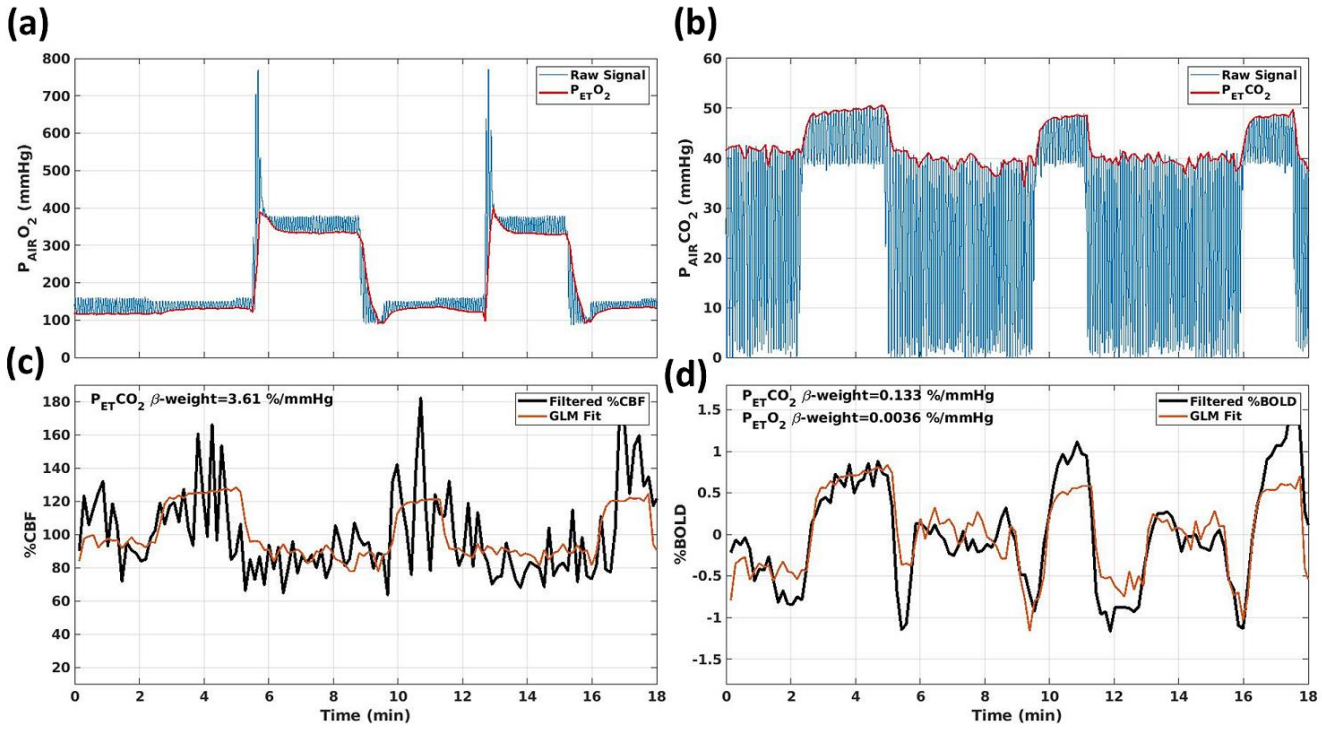

Figure 3: Example of: **(a)** O_2 and estimated $P_{ET}O_2$ traces; **(b)** CO_2 and estimated $P_{ET}CO_2$ traces; **(c)** GM CBF/CBF_0 and fitted $P_{ET}CO_2$ trace. The β-weight of the GLM fit, with units of a CVR, CBF/CBF_0/mmHg, was multiplied by the maximum modulation $\Delta P_{ET}CO_2$ to obtain the hypercapnic CBF/CBF_0. **(d)** GM average $\Delta BOLD/BOLD_0$ and fitted $P_{ET}CO_2$ and $P_{ET}O_2$ traces. The β-weights, with units of %BOLD/mmHg of $P_{ET}CO_2$ and $P_{ET}O_2$, were multiplied by the maximum modulation $\Delta P_{ET}O_2$ and $\Delta P_{ET}O_2$ to obtain the hypercapnic and the hyperoxic $\Delta BOLD/BOLD_0$.

3.2. *In-Vivo* Estimation of Modeling Parameters (Section 2)

Figure 4 reports the analysis performed *in-vivo* to evaluate the modelling parameters. Figure 4a reports the subjects' average value (and standard error, SE) of $A\cdot\rho/k$ as a function of $P_mO_{2,0}$. The value is reported for both hc-fMRI+ and ho-fMRI+. In agreement with Equation 9, for higher $P_mO_{2,0}$ the estimate of $A\cdot\rho/k$ decreased. We obtained, for a $P_mO_{2,0}$=0, an average value of $A\cdot\rho/k$=8.85 $s^{-1}g^{-\beta}dL^{\beta}/(\mu mol/mmHg/ml/min)$ (SE=0.58 $s^{-1}g^{-\beta}dL^{\beta}/(\mu mol/mmHg/ml/min)$) for hc-fMRI+ and $A\cdot\rho/k$=6.03 $s^{-1}g^{-\beta}dL^{\beta}/(\mu mol/mmHg/ml/min)$ (SE=0.41 $s^{-1}g^{-\beta}dL^{\beta}/(\mu mol/mmHg/ml/min)$) for ho-fMRI+. Figure 4b reports the CoV of $A\cdot\rho/k$ for hc-fMRI+ and ho-fMRI+ as a

function of $P_mO_{2,0}$. The smallest CoV was obtained with a $P_mO_{2,0}\approx0$ for both hc-fMRI+ (CoV=0.29) and ho-fMRI+ (CoV=0.31) with a monotonic CoV increase at increasing $P_mO_{2,0}$.

Figure 4c reports the comparison between hc-fMRI+ and ho-fMRI+ estimates of $A\cdot\rho/k$ for each subject, when fixing the $P_mO_{2,0}$ at the value of $P_mO_{2,0}$=0 mmHg . A good correlation was obtained with a r=0.71, df=18, $p=4.2\cdot10^{-4}$, with a smaller hyperoxic estimate.

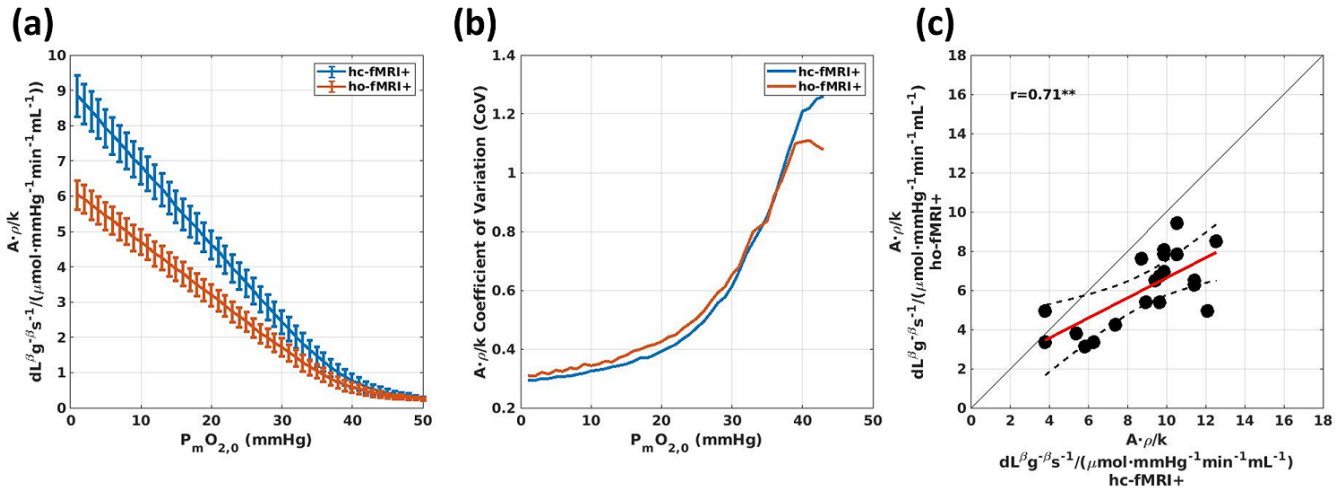

Figure 4: Results of the analysis evaluating the modelling unknown parameters that used hc-fMRI+ or ho-fMRI+ and the OEF_0 derived from the dc-fMRI analysis. **(a)** Subjects' average (and SE) estimate of the scaling parameter $A\cdot\rho/k$ of the model as a function of the $P_mO_{2,0}$ assumed. **(b)** Subjects' CoV of the scaling parameter $A\cdot\rho/k$ as a function of $P_mO_{2,0}$ assumed. **(c)** Comparison between hc-fMRI+ and ho-fMRI+ estimates of $A\cdot\rho/k$ for each subject, assuming a $P_mO_{2,0}$=0 mmHg. ** $p<0.01$

3.3. *In-Vivo* Estimation of Oxygen Extraction Fraction: Calibrated fMRI vs. Dual-Calibrated fMRI (Section 3)

Figure 5a reports exemplar OEF_0 and $CMRO_{2,0}$ maps obtained with dc-fMRI, hc-fMRI+ and ho-fMRI+. Notably, subjects' average spatial variabilities (estimated as standard deviation, SD) in the GM OEF_0 of SD=0.17 (SE=0.003), SD=0.13 (SE=0.002) and SD=0.15 (SE=0.002) were obtained for dc-fMRI, hc-fMRI+ and ho-fMRI+, respectively.

Figure 5b reports the scatterplots and the Bland-Altmann plots comparing the average OEF_0 in the GM between dc-fMRI and the single calibration approaches. Average global GM OEF_0 (mean±SD) were 0.39±0.04, 0.39±0.03, and 0.40±0.03 for dc-fMRI, hc-fMRI+ and ho-fMRI+, respectively. hc-fMRI+

OEF_0 was significantly correlated with that of dc-fMRI (r=0.65, df=18, $p=2\cdot10^{-3}$, OEF_0 RMSE=0.033) whereas that of ho-fMRI+ was not (r=0.26, df=18, p=0.27, OEF_0 RMSE=0.044). No significant bias between the different approaches was found, but this was dependent on the proportionality constant calibration using dc-fMRI. A significant correlation, with no bias, was obtained between hc-fMRI+ and ho-fMRI+ (r=0.50, df=18, p=0.02).

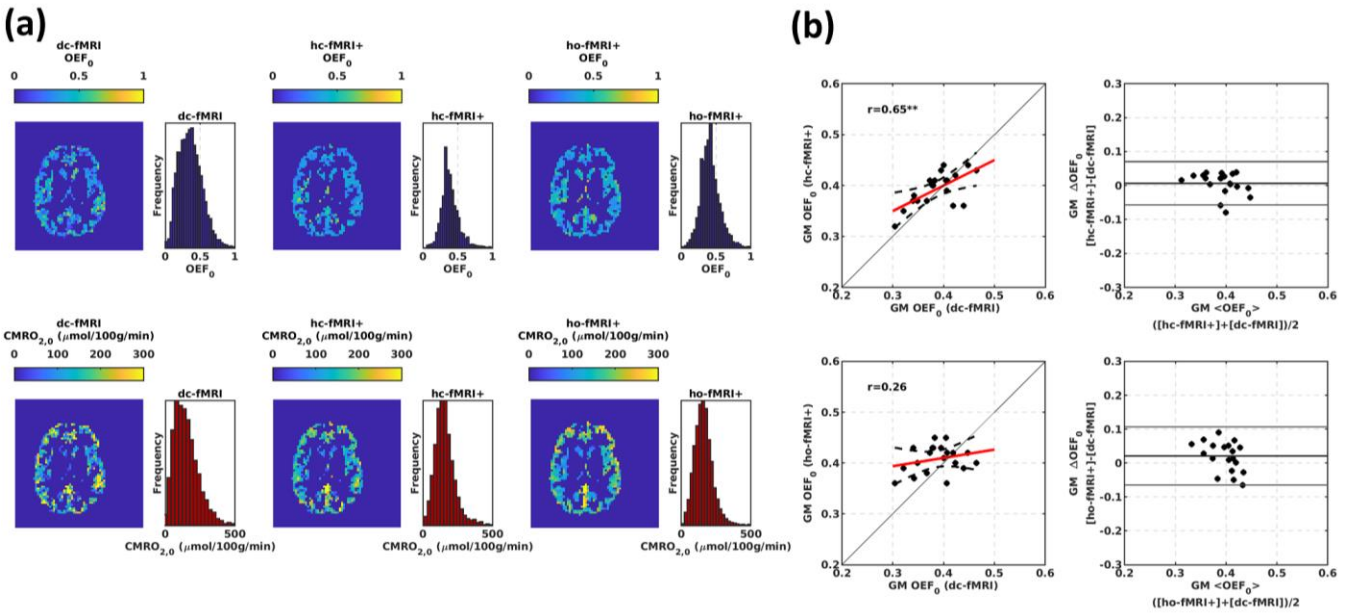

Figure 5: (a) Exemplar GM OEF_0 and $CMRO_{2,0}$ maps for a participant of the study obtained with dc-fMRI (left colum), hc-fMRI+ (central column) and ho-fMRI+ (right column). **(b)** Scatterplots and Bland-Altmann plots comparing the average OEF_0 in the GM between the hc-fMRI+ (upper row) and ho-fmri+ (lower row) and dc-fMRI. **p<0.01; ***$p<10^{-3}$

3.4. *In-Vivo* Estimation of Oxygen Extraction Fraction: Calibrated fMRI vs. OxFlow (Section 4)

Figure 6 reports the scatterplots and the Bland-Altmann plots comparing the global OEF_0 of the fMRI approaches to the OEF_0 estimated in the SSS using OxFlow in a subset of 12 subjects. Figure 6a shows, for one representative subject, the magnitude image and the processed phase image used to estimate OEF_0 in the SSS within OxFlow. Average SSS OEF_0 estimated using OxFlow was 0.31 ± 0.07. Significant associations of the average OEF_0 in the GM using a fMRI approach with whole-brain OEF_0 retrieved using OxFlow were obtained for dc-fMRI (r=0.58, df=10, p=0.048, RMSE=0.034, Figure 6b) and hc-fMRI+ (r=0.64, df=10, p=0.025, Figure 6c,

RMSE=0.041). No significant association was obtained using ho-fMRI+ (r=0.36, df=10, p=0.24, Figure 6d, RMSE=0.066). A systematic bias was obtained with the OxFlow underestimating the OEF_0 with respect to fMRI. For the two fMRI approaches that delivered a significant association with OxFlow, an absolute difference between the dc-fMRI and OxFlow of ΔOEF_0=0.077 with a t=4.57, df=11, $p=8\cdot10^{-4}$, and an absolute difference between hc-fMRI+ and OxFlow OEF_0 of ΔOEF_0=0.083 with a t=5.13, df=11, $p=3.2\cdot10^{-4}$ were obtained.

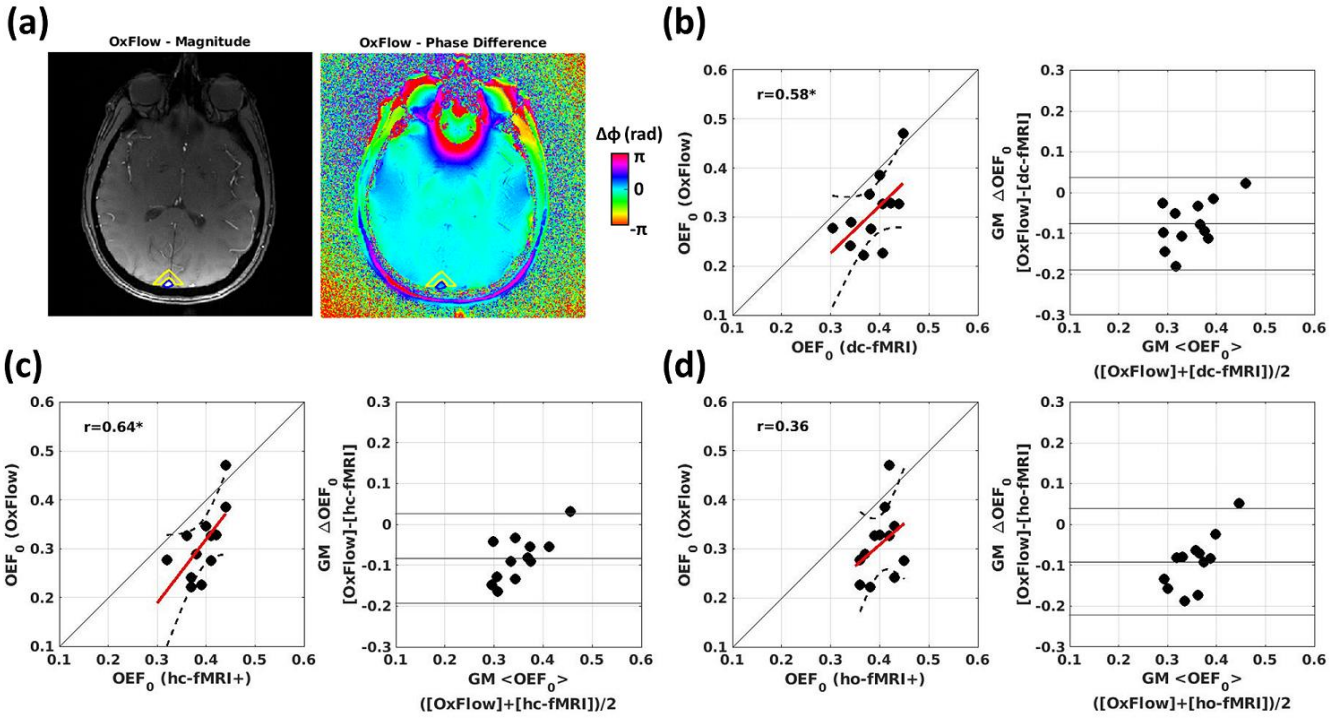

Figure 6: Scatterplots and Bland-Altmann plots comparing the OEF_0 of the calibrated fMRI approaches and OxFlow in a subset of subjects. **(a)** Example of magnitude (arbitrary units) and processed phase images used to estimate OEF_0 in the SSS within the OxFlow method. SSS and the reference region are outlined in blue and yellow, respectively. OxFlow vs. **(b)** dc-fMRI; **(c)** hc-fMRI+; **(d)** ho-fMRI+. * p<0.05

4. Discussion

We introduced a framework for mapping OEF_0 and $CMRO_{2,0}$ using single gas calibrated fMRI. The method integrates a flow-diffusion model of oxygen transport[24] with the steady-state BOLD signal model[16]. Simulations suggest the approach to be valid over a wide range of brain physiology. The new approach, when applied to hypercapnia, compared well with dc-fMRI and whole-brain OEF_0 assessed in the SSS using OxFlow. Compared to dc-fMRI, the novel method permits a simpler stimulation paradigm based on a single exogenous gas challenge[27] or,

presumably, on an endogenous challenge such as breath hold[54], and makes the approach robust to measurement noise.

4.1. Simulations

The simulations relied on a forward model assuming the new framework to be correct. When inverting the model, the unknown random variables were: (i) $A\cdot\rho/k$, a lumped parameter dependent on field strength, tissue structure and vessel geometry and (ii) the mitochondrial oxygen pressure at rest, $P_mO_{2,0}$. Variability in $A\cdot\rho/k$ (CoV=0.3) was based on in-vivo data (Figure 4), whereas the $P_mO_{2,0}$ was simulated in the range 0-$<P_{cap}O_2>$ (Figure 1). When inverting the forward model with these parameters fixed, we obtained low OEF_0 RMSE (around 0.05) for both hc-fMRI+ and ho-fMRI+ when marginalizing all other variables, with slightly better performance for hc-fMRI+ (Figure 2a,b). This highlighted the unknown parameters' reduced effect on the mapping between the measurable variables and OEF_0. In fact, when considering OEF_0 RMSE as a function of a wide range of two interesting physiological variables, $P_mO_{2,0}$ and $MCTT_0$, the OEF_0 RMSE was small. Only with very high $P_mO_{2,0}$ (>25 mmHg) and long $MCTT_0$ (>2.5 s) the RMSE increased significantly. Very high $P_mO_{2,0}$ and long $MCTT_0$, associated with low CBF_0, are expected only in diseases that heavily alter oxygen supply, vasculature and mitochondrial function.

The simulations revealed the effect of BOLD and ASL measurement noise. For both BOLD and ASL modulations, the OEF_0 RMSE quickly reached the value caused by uncertainty in physiology at an SNR≈4. This is the SNR of the modulation estimate, not the temporal SNR of the raw signals. For example, when the modulation is estimated within a GLM framework regressing $P_{ET}O_2$ and $P_{ET}CO_2$ onto BOLD and ASL modulations (Figure 3), the SNR is the GLM β-weight divided by its confidence interval. Average voxel SNRs were between 6 and 16 in vivo for both signals and gas challenges. The robustness to noise of the approach is advantageous compared to dc-fMRI, that often relies on constrained inversion algorithms, trading off accuracy for higher stability[22].

4.2. Modeling Parameters

Investigation of model parameters suggested an average value of $A\cdot\rho/k$ of the order of 10 $s^{-1}g^{-\beta}dL^{\beta}/(\mu mol/mmHg/ml/min)$ when using hc-fMRI+, and an average value of $P_mO_{2,0}$ in the healthy population close to 0 for both hc-fMRI+ and ho-fMRI+ (Figure 4) both results agreed with expectations[36,55]. In fact, the estimate of

$A \cdot \rho/k$ decreased beyond expectations at increasing $PmO_{2,0}$ and increased its CoV as a function of the assumed $PmO_{2,0}$, with a rapid increase above 20 mmHg. This work indeed suggests a particularly low average PmO2,0 in the healthy brain. However, it should be stressed that a strong increase in CoV of $A \cdot \rho/k$ was only observed at PmO2,0 above 20 mmHg. The confidence interval of the estimate still cannot provide a definitive answer on the average PmO2,0 within the range 0-20 mmHg. There is work suggesting the mitochondrial PmO2,0 is about ~12 mmHg[56,57] which goes against the common assumption of $PmO_{2,0}$ being near zero in the healthy brain[36] and, indeed, this is still an open debate. Nonetheless, the simulations of the study clearly demonstrate that the approach estimating OEF_0 has limited sensitivity to the value of $PmO_{2,0}$ if $PmO_{2,0}$ and $MCTT_0$ are not both very high. The good correlation between the hypercapnic and the hyperoxic estimates indicated consistency. However, we obtained a value of $A \cdot \rho/k$ for ho-fMRI+ around 30% smaller than expected. This result might be a cross-talk effect of the hypercapnic on the hyperoxic BOLD modulations in the dc-fMRI experiment, or an overestimation of ΔPaO_2.

4.3. Comparison with dc-fMRI and OxFlow

Spatial homogeneity of OEF_0 in healthy subjects is often taken as an indicator of successful OEF_0 mapping. hc-fMRI+ and ho-fMRI+ decreased OEF_0 spatial variability in GM compared to dc-fmri. The lower variability of hc-fMRI+ and ho-fMRI+ suggests a greater robustness, with respect to measurement SNR, compared to the dc-fMRI. Comparison of GM OEF_0 estimates suggests that hc-fMRI+ is a valid alternative to dc-fMRI (Figure 5b). In addition, when comparing GM OEF_0 of the different fMRI approaches with global OEF_0 in the SSS through OxFlow, clear associations with the OxFlow OEF_0 were obtained for both dc-fMRI and hc-fMRI+ (Figure 6). We identified a bias between the OxFlow and the fMRI estimates. In general, OxFlow OEF_0 yielded a lower value. This is in accordance with the literature, where approaches using analytical modelling give higher estimates of venous saturation[58]. The low performance of ho-fMRI+ is indeed a negative result of the study. Hyperoxia is generally better tolerated than hypercapnia[19] and it would be more easily applicable in clinical settings. The lower performance of hyperoxia is plausibly related to the noisier estimate of M. Moreover, hyperoxic BOLD modulation is primarily sensitive to $CBV_{v,0}$ and largely insensitive to OEF_0; in fact, hyperoxia can be used to estimate $CBV_{v,0}$[59]. The oxygen saturation change due to hyperoxia stimulus is independent of the baseline oxygen saturation over most of the physiological range. In contrast, the oxygen saturation change to a hypercapnic challenge is linearly related

to the resting saturation. The sensitivity pattern of the hyperoxic modulation makes the estimation of OEF_0 with the new framework completely reliant on the flow-diffusion model approximations that link $CBV_{v,0}$ to OEF_0. The model approximations are indeed less influential with hypercapnia, which has a larger sensitivity to OEF_0 with respect to $CBV_{v,0}$, making the hypercapnia approach less noisy and biased.

4.4. Limitations of the Method

The main limitations of the new method are mostly shared with dc-fMRI[14]. The approach using hypercapnia relies on a local CBF increase, a vascular reserve, which may be absent in diseases such ischemic stroke, where vessels may be maximally dilated in an attempt to maintain perfusion. In addition, the method might be vulnerable to larger than expected changes in ρ or k, which are probably not independent. Although large changes in these parameters appear unlikely in many brain diseases, we might expect relevant tissue and vascular remodeling in some disease, such as brain tumors[60]. The limitations of the approach in diseases with concurrent very high $P_mO_{2,0}$ and long $MCTT_0$ are noted earlier and should be assessed in future studies.

4.5. Study Limitations

The main limitation of the simulation study lies in the assumption of an exact analytical model with the error in the estimate of OEF_0 being introduced only by the limited number of measurable variables. The main simplifying assumption of the model was the replacement of the CTT in one straight capillary with the MCTT in the voxel capillary bed. This is an approximation, since, due to the non-linear mapping between CTT, OEF and oxygen diffusion between capillary and tissue, the complete CTT distribution within a capillary bed affects the macroscopic OEF[61]. Without changing MCTT, OEF can be increased through homogenization of the CTT among capillaries. Future extension of the model might include the CTT heterogeneity (CTTH), a measure of the second moment of the CTT distribution within the capillary bed[62].

With respect to the *in-vivo* validation using dc-fMRI, a limiting factor was related to the investigation of the proposed model proportionality constant $A\cdot\rho/k$ and $P_mO_{2,0}$. These estimates were evaluated assuming the OEF_0 derived from the dc-fMRI machine learning analysis[22] to be exact. In fact, noise in the dc-fMRI OEF_0 limited our investigation of the model parameters to global evaluation within the GM. Moreover, another limitation was the problem of having two unknowns and one equation. By exploiting the different effects of these parameters on the

non-linear mapping between variables, we were able to get insight into both parameters, however only at a between subjects' average level. Alternative approaches should be used to investigate the different physiological parameters (e.g., ρ and k) contributing to the proportionality constant, which cannot be separately investigated using standard fMRI approaches. Comparison against non-MRI technology would be essential for definitive validation of the approach. Future validation is also necessary beyond the healthy controls involved in the study, to populations affected by diseases that might alter brain metabolism and for which the proposed model's validity might reduce.

5. Conclusion

We introduced a novel calibrated fMRI framework integrating a steady-state flow-diffusion model of oxygen transport in the BOLD signal model. The simple oxygen transport model assumes the rate of oxygen loss from the capillary is proportional to the $MCTT_0$ and the pressure gradient between capillaries and mitochondria. Since $MCTT_0$ can be expressed as a function of CBVv,0 and CBF_0, and capillary pressure can be expressed as a function of OEF_0, the approach substitutes $CBV_{v,0}$ within the BOLD modelling with a function of CBF_0 and OEF_0 and allows us to estimate OEF_0 using a single manipulation of brain physiology.

Uncertainty in the integrated model was driven by variability in two non-measurable parameters, a proportionality constant $A \cdot \rho/k$, that depended on tissue and microvascular structure at a fixed field strength, and $PmO_{2,0}$. The advantage of the new framework lies in the low variability of these parameters and their limited influence on the OEF_0 estimation compared to CBVv,0. Even by fixing these parameters to plausible values, the simulations showed the OEF0 RMSE to be below 0.05 over a wide range of physiology meaning that the method may reliably identify OEF_0 modifications greater than approximately 10%. Only with concurrently very high $PmO_{2,0}$ (>25 mmHg) and long $MCTT_0$ (>2.5 s) the RMSE increased significantly. Importantly, the approach was highly robust to measurement noise. The method, when using hypercapnia in vivo, compared well with dc-fMRI and with whole-brain OEF derived from macrovascular susceptibility measures in the superior sagittal sinus using the OxFlow method. Lack of positive results when using hyperoxia may be related to the high sensitivity to $CBV_{v,0}$

and poor sensitivity to OEF_0. The simplified calibrated fMRI method using hypercapnia has potential for application in clinical settings.

Acknowledgments: This work was partially conducted under the framework of the Departments of Excellence 2018–2022 initiative of the Italian Ministry of Education, University and Research for the Department of Neuroscience, Imaging and Clinical Sciences (DNISC) of the University of Chieti-Pescara, Italy. MG thanks the Wellcome Trust for its support via a Sir Henry Dale Fellowship (220575/Z/20/Z). This project was partially supported by the UK Engineering and Physical Sciences Research Council (EP/S025901/1). This work was supported by the National Institute of Health (P41-EB029460). HLC and MG were funded by a Wellcome Strategic Award to CUBRIC, 'Multi-scale and multi-modal assessment of coupling in the healthy and diseased brain' (104943/Z/14/Z). RCS, EP and CF were supported by Wellcome PhD studentships. KM was supported by a Wellcome Senior Research Fellowship, "Assessing the health of ageing blood vessels in the brain using fMRI" (200804/Z/16/Z). The study was partially supported by the MS Society UK.

Author contribution statement: AMC and MG developed imaging and analysis methods, and analyzed and interpreted the data. AMC, MG and RGW drafted the manuscript. FWW, RGW, KM and VT conceived the project. MG, HLC, RCS, EP, NS, SK, SJ, CF and KM set up and executed the experiment. DM, EB, AERS and EE contributed to data analysis. All authors revised and approved the final submission.

Competing Interests: The authors declare no competing financial and non-financial interests.

Data availability statement: The data that support the findings of this study are available upon reasonable request.

Supplementary information: Supplementary information is available on JCBFM website.

References

1 Magistretti P, Allaman I. Brain energy metabolism. *Neurosci 21st Century Basic Clin* 2013; : 1591–1620.

2 Barhoum S, Langham MC, Magland JF, Rodgers ZB, Li C, Rajapakse CS *et al.* Method for Rapid MRI Quantification of Global Cerebral Metabolic Rate of Oxygen. *J Cereb Blood Flow Metab* 2015; **35**: 1616–1622.

3 Bolar DS, Rosen BR, Sorensen AG, Adalsteinsson E. QUantitative Imaging of eXtraction of oxygen and TIssue consumption (QUIXOTIC) using venular-targeted velocity-selective spin labeling. *Magn Reson Med* 2011; **66**: 1550–1562.

4 Bulte DP, Kelly M, Germuska M, Xie J, Chappell MA, Okell TW *et al.* Quantitative measurement of cerebral physiology using respiratory-calibrated MRI. *NeuroImage* 2012; **60**: 582–591.

5 Fan AP, Govindarajan ST, Kinkel RP, Madigan NK, Nielsen AS, Benner T *et al.* Quantitative Oxygen Extraction Fraction from 7-Tesla MRI Phase: Reproducibility and Application in Multiple Sclerosis. *J Cereb Blood Flow Metab* 2015; **35**: 131–139.

6 Guo J, Wong EC. Venous oxygenation mapping using velocity-selective excitation and arterial nulling. *Magn Reson Med* 2012; **68**: 1458–1471.

7 He X, Yablonskiy DA. Quantitative BOLD: Mapping of human cerebral deoxygenated blood volume and oxygen extraction fraction: Default state. *Magn Reson Med* 2007; **57**: 115–126.

8 Lu H, Xu F, Grgac K, Liu P, Qin Q, Zijl P van. Calibration and validation of TRUST MRI for the estimation of cerebral blood oxygenation. *Magn Reson Med* 2012; **67**: 42–49.

9 Barhoum S, Rodgers ZB, Langham M, Magland JF, Li C, Wehrli FW. Comparison of MRI methods for measuring whole-brain venous oxygen saturation. *Magn Reson Med* 2015; **73**: 2122–2128.

10 He X, Zhu M, Yablonskiy DA. Validation of oxygen extraction fraction measurement by qBOLD technique. *Magn Reson Med* 2008; **60**: 882–888.

11 Zhang J, Liu T, Gupta A, Spincemaille P, Nguyen TD, Wang Y. Quantitative mapping of cerebral metabolic rate of oxygen (CMRO2) using quantitative susceptibility mapping (QSM). *Magn Reson Med* 2015; **74**: 945–952.

12 Gauthier CJ, Hoge RD. Magnetic resonance imaging of resting OEF and $CMRO_2$ using a generalized calibration model for hypercapnia and hyperoxia. *NeuroImage* 2012; **60**: 1212–1225.

13 Germuska M, Chandler HL, Stickland RC, Foster C, Fasano F, Okell TW *et al.* Dual-calibrated fMRI measurement of absolute cerebral metabolic rate of oxygen consumption and effective oxygen diffusivity. *NeuroImage* 2019; **184**: 717–728.

14 Germuska M, Wise RG. Calibrated fMRI for mapping absolute CMRO2: Practicalities and prospects. *NeuroImage* 2019; **187**: 145–153.

15 Wise RG, Harris AD, Stone AJ, Murphy K. Measurement of OEF and absolute CMRO2: MRI-based methods using interleaved and combined hypercapnia and hyperoxia. *NeuroImage* 2013; **83**: 135–147.

16 Davis TL, Kwong KK, Weisskoff RM, Rosen BR. Calibrated functional MRI: Mapping the dynamics of oxidative metabolism. *Proc Natl Acad Sci* 1998; **95**: 1834–1839.

17 Champagne AA, Coverdale NS, Germuska M, Bhogal AA, Cook DJ. Changes in volumetric and metabolic parameters relate to differences in exposure to sub-concussive head impacts. *J Cereb Blood Flow Metab* 2020; **40**: 1453–1467.

18 De Vis JB, Petersen ET, Bhogal A, Hartkamp NS, Klijn CJ, Kappelle L *et al.* Calibrated MRI to Evaluate Cerebral Hemodynamics in Patients with an Internal Carotid Artery Occlusion. *J Cereb Blood Flow Metab* 2015; **35**: 1015–1023.

19 Lajoie I, Nugent S, Debacker C, Dyson K, Tancredi FB, Badhwar A *et al.* Application of calibrated fMRI in Alzheimer's disease. *NeuroImage Clin* 2017; **15**: 348–358.

20 Merola A, Germuska MA, Murphy K, Wise RG. Assessing the repeatability of absolute CMRO2, OEF and haemodynamic measurements from calibrated fMRI. *NeuroImage* 2018; **173**: 113–126.

21 Merola A, Germuska MA, Warnert EA, Richmond L, Helme D, Khot S *et al.* Mapping the pharmacological modulation of brain oxygen metabolism: The effects of caffeine on absolute CMRO2 measured using dual calibrated fMRI. *NeuroImage* 2017; **155**: 331–343.

22 Germuska M, Chandler HL, Okell T, Fasano F, Tomassini V, Murphy K *et al.* A Frequency-Domain Machine Learning Method for Dual-Calibrated fMRI Mapping of Oxygen Extraction Fraction (OEF) and Cerebral Metabolic Rate of Oxygen Consumption (CMRO2). *Front Artif Intell* 2020; **3**. doi:10.3389/frai.2020.00012.

23 Gjedde A. Cerebral Blood Flow Change in Arterial Hypoxemia Is Consistent with Negligible Oxygen Tension in Brain Mitochondria. *NeuroImage* 2002; **17**: 1876–1881.

24 Hayashi T, Watabe H, Kudomi N, Kim KM, Enmi J-I, Hayashida K *et al.* A theoretical model of oxygen delivery and metabolism for physiologic interpretation of quantitative cerebral blood flow and metabolic rate of oxygen. *J Cereb Blood Flow Metab Off J Int Soc Cereb Blood Flow Metab* 2003; **23**: 1314–1323.

25 Lee H, Langham MC, Rodriguez-Soto AE, Wehrli FW. Multiplexed MRI methods for rapid estimation of global cerebral metabolic rate of oxygen consumption. *NeuroImage* 2017; **149**: 393–403.

26 Boxerman JL, Bandettini PA, Kwong KK, Baker JR, Davis TL, Rosen BR *et al.* The intravascular contribution to fmri signal change: monte carlo modeling and diffusion-weighted studies in vivo. *Magn Reson Med* 1995; **34**: 4–10.

27 Hoge RD, Atkinson J, Gill B, Crelier GR, Marrett S, Pike GB. Investigation of BOLD signal dependence on cerebral blood flow and oxygen consumption: The deoxyhemoglobin dilution model. *Magn Reson Med* 1999; **42**: 849–863.

28 Buxton RB. *Introduction to Functional Magnetic Resonance Imaging: Principles and Techniques*. Cambridge University Press, 2009.

29 Germuska M, Merola A, Murphy K, Babic A, Richmond L, Khot S *et al.* A forward modelling approach for the estimation of oxygen extraction fraction by calibrated fMRI. *NeuroImage* 2016; **139**: 313–323.

30 Hyder F, Shulman RG, Rothman DL. A model for the regulation of cerebral oxygen delivery. *J Appl Physiol* 1998; **85**: 554–564.

31 Ogawa S, Menon RS, Tank DW, Kim SG, Merkle H, Ellermann JM *et al.* Functional brain mapping by blood oxygenation level-dependent contrast magnetic resonance imaging. A comparison of signal characteristics with a biophysical model. *Biophys J* 1993; **64**: 803–812.

32 Blockley NP, Griffeth VEM, Buxton RB. A general analysis of calibrated BOLD methodology for measuring CMRO2 responses: Comparison of a new approach with existing methods. *NeuroImage* 2012; **60**: 279–289.

33 Blockley NP, Griffeth VEM, Simon AB, Dubowitz DJ, Buxton RB. Calibrating the BOLD response without administering gases: Comparison of hypercapnia calibration with calibration using an asymmetric spin echo. *NeuroImage* 2015; **104**: 423–429.

34 Blockley NP, Stone AJ. Improving the specificity of R2′ to the deoxyhaemoglobin content of brain tissue: Prospective correction of macroscopic magnetic field gradients. *NeuroImage* 2016; **135**: 253–260.

35 Hua J, Liu P, Kim T, Donahue M, Rane S, Chen JJ *et al.* MRI techniques to measure arterial and venous cerebral blood volume. *NeuroImage* 2019; **187**: 17–31.

36 Gjedde A, Poulsen PH, Østergaard L. On the Oxygenation of Hemoglobin in the Human Brain. In: Eke A, Delpy DT (eds). *Oxygen Transport to Tissue XXI*. Springer US: Boston, MA, 1999, pp 67–81.

37 Gjedde A, Johannsen P, Cold GE, Østergaard L. Cerebral Metabolic Response to Low Blood Flow: Possible Role of Cytochrome Oxidase Inhibition. *J Cereb Blood Flow Metab* 2005; **25**: 1183–1196.

38 Okell TW, Chappell MA, Kelly ME, Jezzard P. Cerebral Blood Flow Quantification Using Vessel-Encoded Arterial Spin Labeling. *J Cereb Blood Flow Metab* 2013; **33**: 1716–1724.

39 Schmithorst VJ, Hernandez-Garcia L, Vannest J, Rajagopal A, Lee G, Holland SK. Optimized Simultaneous ASL and BOLD Functional Imaging of the Whole Brain. *J Magn Reson Imaging JMRI* 2014; **39**: 1104–1117.

40 Jain V, Langham MC, Wehrli FW. MRI Estimation of Global Brain Oxygen Consumption Rate. *J Cereb Blood Flow Metab* 2010; **30**: 1598–1607.

41 Langham MC, Magland JF, Epstein CL, Floyd TF, Wehrli FW. Accuracy and precision of MR blood oximetry based on the long paramagnetic cylinder approximation of large vessels. *Magn Reson Med* 2009; **62**: 333–340.

42 Langham MC, Magland JF, Floyd TF, Wehrli FW. Retrospective correction for induced magnetic field inhomogeneity in measurements of large-vessel hemoglobin oxygen saturation by MR susceptometry. *Magn Reson Med* 2009; **61**: 626–633.

43 Gai X, Taki K, Kato H, Nagaishi H. Regulation of hemoglobin affinity for oxygen by carbonic anhydrase. *J Lab Clin Med* 2003; **142**: 414–420.

44 Jenkinson M, Beckmann CF, Behrens TEJ, Woolrich MW, Smith SM. FSL. *NeuroImage* 2012; **62**: 782–790.

45 Jenkinson M, Bannister P, Brady M, Smith S. Improved optimization for the robust and accurate linear registration and motion correction of brain images. *NeuroImage* 2002; **17**: 825–841.

46 Smith SM. Fast robust automated brain extraction. *Hum Brain Mapp* 2002; **17**: 143–155.

47 Zhang Y, Brady M, Smith S. Segmentation of brain MR images through a hidden Markov random field model and the expectation-maximization algorithm. *IEEE Trans Med Imaging* 2001; **20**: 45–57.

48 Alsop DC, Detre JA, Golay X, Günther M, Hendrikse J, Hernandez-Garcia L *et al.* Recommended implementation of arterial spin-labeled perfusion MRI for clinical applications: A consensus of the ISMRM perfusion study group and the European consortium for ASL in dementia. *Magn Reson Med* 2015; **73**: 102–116.

49 Mutsaerts HJMM, Steketee RME, Heijtel DFR, Kuijer JPA, Osch MJP van, Majoie CBLM *et al.* Inter-Vendor Reproducibility of Pseudo-Continuous Arterial Spin Labeling at 3 Tesla. *PLOS ONE* 2014; **9**: e104108.

50 Pilkinton DT, Hiraki T, Detre JA, Greenberg JH, Reddy R. Absolute cerebral blood flow quantification with pulsed arterial spin labeling during hyperoxia corrected with the simultaneous measurement of the longitudinal relaxation time of arterial blood. *Magn Reson Med* 2012; **67**: 1556–1565.

51 Friston KJ. Statistical parametric mapping. In: *Functional neuroimaging: Technical foundations*. Academic Press: San Diego, CA, US, 1994, pp 79–93.

52 Insiripong S, Supattarobol T, Jetsrisuparb A. Comparison of hematocrit/hemoglobin ratios in subjects with alpha-thalassemia, with subjects having chronic kidney disease and normal subjects. *Southeast Asian J Trop Med Public Health* 2013; **44**: 707–711.

53 Spees WM, Yablonskiy DA, Oswood MC, Ackerman JJH. Water proton MR properties of human blood at 1.5 Tesla: Magnetic susceptibility, T1, T2, T, and non-Lorentzian signal behavior. *Magn Reson Med* 2001; **45**: 533–542.

54 Kastrup A, Krüger G, Neumann-Haefelin T, Moseley ME. Assessment of cerebrovascular reactivity with functional magnetic resonance imaging: comparison of CO2 and breath holding. *Magn Reson Imaging* 2001; **19**: 13–20.

55 Germuska M, Stickland RC, Chiarelli AM, Chandler HL, Wise RG. Quantitative mapping of cerebral oxygen metabolism using breath-hold calibrated fMRI. *bioRxiv* 2021; : 2021.04.08.438939.

56 Wilson DF. Regulation of cellular metabolism: programming and maintaining metabolic homeostasis. *J Appl Physiol* 2013; **115**: 1583–1588.

57 Buxton RB. The thermodynamics of thinking: connections between neural activity, energy metabolism and blood flow. *Philos Trans R Soc B Biol Sci* 2021; **376**: 20190624.

58 Driver ID, Wharton SJ, Croal PL, Bowtell R, Francis ST, Gowland PA. Global intravascular and local hyperoxia contrast phase-based blood oxygenation measurements. *NeuroImage* 2014; **101**: 458–465.

59 Blockley NP, Griffeth VEM, Germuska MA, Bulte DP, Buxton RB. An analysis of the use of hyperoxia for measuring venous cerebral blood volume: Comparison of the existing method with a new analysis approach. *NeuroImage* 2013; **72**: 33–40.

60 Owen MR, Alarcón T, Maini PK, Byrne HM. Angiogenesis and vascular remodelling in normal and cancerous tissues. *J Math Biol* 2008; **58**: 689.

61 Li Y, Wei W, Wang RK. Capillary flow homogenization during functional activation revealed by optical coherence tomography angiography based capillary velocimetry. *Sci Rep* 2018; **8**: 4107.

62 Jespersen SN, Østergaard L. The Roles of Cerebral Blood Flow, Capillary Transit Time Heterogeneity, and Oxygen Tension in Brain Oxygenation and Metabolism. *J Cereb Blood Flow Metab* 2012; **32**: 264–277.

Tables

Abbreviation	Meaning	Units	Abbreviation	Meaning	Units
$_0$	As subscript defines the physiological variable at baseline	/	**[Hb]**	Concentration of hemoglobin in blood	g/dL
α	Grubb exponent relating fractional change in CBV_v to fractional change in CBF	Dimensionless	**β**	Field strength and vessel geometry dependent exponent within the steady-state BOLD signal model	Dimensionless
β-weight	Coefficient of the GLM	/	**γ**	Gyromagnetic ratio of the proton	rad/s/T
$\Delta\chi_{do}$	Magnetic susceptibility difference between fully oxygenated and fully deoxygenated blood	Relative	**$\Delta BOLD/BOLD_0$**	Relative change in BOLD signal	Relative
ΔS	Tag-Control ASL image	Not defined	**ε**	Oxygen plasma solubility	mL/mmHg/dL
η	Tagging inversion efficiency of PCASL	Dimensionless	**η_{INV}**	Scaling factor accounting for reduction in tagging efficiency due to background suppression	Dimensionless
λ	Water partition coefficient of the tissue	mL/g	**ρ**	$CBV_{v,0}/CBV_{cap,0}$	Relative
φ	Oxygen binding capacity of hemoglobin	mL/g	**Φ**	Phase MRI image	rad
τ	Labelling duration of PCASL	s	**A**	Field strength and vessel geometry dependent proportionality constant within the steady-state BOLD signal model	$s^{-1}g^{-\beta}dL^{\beta}$
ASL	Arterial spin labelling	/	**B_0**	Static magnetic field	T
BOLD	Blood oxygen level dependent	Not Defined	**C_aO_2**	Concentration of oxygen in arteries	mL/dL
CBF	Cerebral blood flow	mL/100g/min	**CBF/CBF_0**	Fractional change in CBF	Relative
CBV_{cap}	Capillary blood volume	Relative (or ml/100g)	**CBV_v**	dHb-sensitive blood volume	Relative (or ml/100g)
$CMRO_2$	Cerebral metabolic rate of oxygen	μmol/100g/min	**$CBV_v/CBV_{v,0}$**	Fractional change in CBV_v	Relative
CSF	Cerebrospinal fluid	/	**CTT**	Capillary transit time	s
CoV	Coefficient of variation	Relative	**CVR**	Cerebrovascular reactivity (CBF/CBF_0/mmHg of CO_2)	%/mmHg
dc-fMRI	Dual-Calibrated functional MRI	/	**dHb**	Deoxy-hemoglobin concentration in tissue	g/100g
GLM	General Linear Model	/	**GM**	Grey matter	/
GRE	Gradient Echo Sequence	/	**k**	Effective permeability to oxygen of the capillary endothelium and brain tissue	μmol/mmHg/mL/min
h	Hill constant involved in the non-linear relationship between oxygen partial pressure and hemoglobin saturation in blood	Dimensionless	**hc-fMRI+**	Single gas calibrated fMRI using a hypercapnic modulation and the steady-state BOLD signal model extended with the proposed flow-diffusion analytical framework of oxygen transport	/

hc-fMRI	Single gas calibrated fMRI using a hypercapnic modulation and the steady-state BOLD signal model	/	**Hct**	Hematocrit	%
ho-fMRI+	Single gas calibrated fMRI using a hyperoxic modulation and the steady-state BOLD signal model extended with the proposed flow-diffusion analytical framework of oxygen transport		**ho-fMRI**	Single gas calibrated fMRI using a hyperoxic modulation and the steady-state BOLD signal model	/
MCTT	Mean capillary transit time	s	**M**	Maximum BOLD modulation	Relative
OxFlow	Validated macrovascular global measure of OEF_0, inferred through phase measures of the magnetic susceptibility of blood in the sagittal sinus relative to surrounding tissue	/	**OEF**	Oxygen Extraction Fraction	Relative
$\mathbf{P_{50}}$	Oxygen partial pressure when half of hemoglobin is saturated with oxygen	mmHg	$\mathbf{P_aO_2}$	Partial pressure of oxygen in arteries	mmHg
$\mathbf{P_aCO_2}$	Partial pressure of carbon dioxide in arteries	mmHg	$\mathbf{P_{cap}O_2}$	Partial pressure of oxygen in the capillary	mmHg
PCASL	Pseudo-continuous ASL	/	$\mathbf{P_{ET}O_2}$	End-tidal partial pressure of oxygen	mmHg
$\mathbf{P_{ET}CO_2}$	End-tidal partial pressure of carbon dioxide	mmHg	$\mathbf{P_mO_2}$	Partial pressure of oxygen at the mitochondria	mmHg
PLD	Post label delay of PCASL	s	$\mathbf{R_2^*|_{dHb}}$	Rate of free induction decay due to dHb	1/s
RMSE	Root mean square error	Variable	$\mathbf{S_0}$	Proton Density Image for ASL normalization	Not defined
$\mathbf{S_{cap}O_2}$	Capillary oxygen saturation of hemoglobin	Relative	$\mathbf{S_aO_2}$	Arterial oxygen saturation of hemoglobin	Relative
SD	Standard deviation	Variable	**SE**	Standard error (standard deviation of the mean)	Variable
$\mathbf{S_vO_2}$	Venous oxygen saturation of hemoglobin	Relative	**SNR**	Signal to Noise Ratio	Dimensionless
SSS	Superior Sagittal Sinus	/	$\mathbf{T1_b}$	MRI longitudinal relaxation time constant of blood	s
TE	Time of echo of the MRI sequence	s	**TOF**	Time of flight MRI	/
TR	Time of repetition of the MRI sequence		**WM**	White matter	/

Table 1: Main variables and abbreviations used in the study, reported in alphabetical order.

Figure Legends

Figure 1: Random variables used to simulate BOLD and ASL signals using a hc-fMRI+ or ho-fMRI+ forward modelling framework. The variables reported in light grey were assumed to be measured for the hc-fMRI+ or ho-fMRI+ inversion model, those reported in medium grey were fixed a-priori in the inversion model and those in dark grey were inferred by the inversion model.

Figure 2: (a) RMSE in OEF_0 for hc-fMRI+ and ho-fMRI+ inversion models with $A{\cdot}\rho/k=10\ s^{-1}g^{-\beta}dL^{\beta}/(\mu mol/mmHg/ml/min)$ as a function of $P_mO_{2,0}$. **(b)** Scatterplots of the simulated and estimated OEF_0 for hc-fMRI+ and ho-fMRI+ inversion models assuming either $P_mO_{2,0}$=0 mmHg or $P_mO_{2,0}$=10 mmHg; **(c)** RMSE in OEF_0 as a function of the forward model $MCTT_0$ and $P_mO_{2,0}$ for hc-fMRI+ and ho-fMRI+ inversion models assuming either $P_mO_{2,0}$=0 mmHg or $P_mO_{2,0}$=10 mmHg. *** $p<10^{-3}$

Figure 3: Example of: **(a)** O_2 and estimated $P_{ET}O_2$ traces; **(b)** CO_2 and estimated $P_{ET}CO_2$ traces; **(c)** GM CBF/CBF_0 and fitted $P_{ET}CO_2$ trace. The β-weight of the GLM fit, with units of a CVR, CBF/CBF_0/mmHg, was multiplied by the maximum modulation $\Delta P_{ET}CO_2$ to obtain the hypercapnic CBF/CBF_0. **(d)** GM average $\Delta BOLD/BOLD_0$ and fitted $P_{ET}CO_2$ and $P_{ET}O_2$ traces. The β-weights, with units of %BOLD/mmHg of $P_{ET}CO_2$ and $P_{ET}O_2$, were multiplied by the maximum modulation $\Delta P_{ET}O_2$ and $\Delta P_{ET}O_2$ to obtain the hypercapnic and the hyperoxic $\Delta BOLD/BOLD_0$.

Figure 4: Results of the analysis evaluating the modelling unknown parameters that used hc-fMRI+ or ho-fMRI+ and the OEF_0 derived from the dc-fMRI analysis. **(a)** Subjects' average (and SE) estimate of the scaling parameter $A{\cdot}\rho/k$ of the model as a function of the $P_mO_{2,0}$ assumed. **(b)** Subjects' CoV of the scaling parameter $A{\cdot}\rho/k$ as a function of $P_mO_{2,0}$ assumed. **(c)** Comparison between hc-fMRI+ and ho-fMRI+ estimates of $A{\cdot}\rho/k$ for each subject, assuming a $P_mO_{2,0}$=0 mmHg. ** $p<0.01$

Figure 5: (a) Exemplar GM OEF_0 and $CMRO_{2,0}$ maps for a participant of the study obtained with dc-fMRI (left colum), hc-fMRI+ (central column) and ho-fMRI+ (right column). **(b)** Scatterplots and Bland-Altmann plots comparing the average OEF_0 in the GM between the hc-fMRI+ (upper row) and ho-fmri+ (lower row) and dc-fMRI. **$p<0.01$; ***$p<10^{-3}$

Figure 6: Scatterplots and Bland-Altmann plots comparing the OEF_0 of the calibrated fMRI approaches and OxFlow in a subset of subjects. **(a)** Example of magnitude (arbitrary units) and processed phase images used to estimate OEF_0 in the SSS within the OxFlow method. SSS and the reference region are outlined in blue and yellow, respectively. OxFlow vs. **(b)** dc-fMRI; **(c)** hc-fMRI+; **(d)** ho-fMRI+. * $p<0.05$